Towards modelling ghostly damped Ly αs

Brivael Laloux[1,2]⋆ and Patrick Petitjean[3]⋆

[1]*Centre for Extragalactic Astronomy, Department of Physics, Durham University, Durham DH1 3LE, UK*
[2]*National Observatory of Athens, V. Paulou & I. Metaxa, Metaxa 11532, Greece*
[3]*Institut d'Astrophysique de Paris, Sorbonne Universités and CNRS, 98bis Boulevard Arago, F-75014 Paris, France*

ABSTRACT

We use simple models of the spatial structure of the quasar broad-line region (BLR) to investigate the properties of so-called *ghostly* damped Ly α (DLA) systems detected in Sloan Digital Sky Survey (SDSS) data. These absorbers are characterized by the presence of strong metal lines but no H I Ly α trough is seen in the quasar spectrum indicating that, although the region emitting the quasar continuum is covered by an absorbing cloud, the BLR is only partially covered. One of the models has a spherical geometry, another one is the combination of two wind flows, whereas the third model is a Keplerian disc. The models can reproduce the typical shape of the quasar Ly α emission and different *ghostly* configurations. We show that the DLA H I column density can be recovered precisely independently of the BLR model used. The size of the absorbing cloud and its distance to the centre of the AGN are correlated. However, it may be possible to disentangle the two using an independent estimate of the radius from the determination of the particle density. Comparison of the model outputs with SDSS data shows that the wind and disc models are more versatile than the spherical one and can be more easily adapted to the observations. For all the systems, we derive $\log N(\text{H I})(\text{cm}^{-2}) > 20.5$. With higher quality data, it may be possible to distinguish between the models.

Key words: quasars: absorption lines – quasars: emission lines.

1 INTRODUCTION

One of the most challenging issues in quasar physics is to understand how black holes are fed with infalling gas. The infall of gas on to the host-galaxy occurs preferentially through cold streams along the filaments of the cosmic web (van de Voort et al. 2012). So far, no direct robust observational evidence has been found for the existence of this infalling gas (Christensen et al. 2006; O'Sullivan et al. 2020). Instead, outflows driven by active galactic nuclei (AGN) are ubiquitously observed as blueshifted absorption features in quasar spectra at any redshift (Rankine et al. 2020).

The infalling gas must be compressed when reaching the disc of the galaxy and the compressed gas could give rise to a DLA in the quasar spectrum. Since the DLA and the background quasar are located at almost the same redshift, the DLA can act as a natural coronagraph, blocking the quasar blazing radiation in Ly α. This can allow us, depending on the dimension of these so-called *eclipsing* DLAs, to detect fainter emission from star-forming regions in the host galaxy and the extended quasar halo and/or to observe the narrow-line region (NLR) of the AGN. The leaked emission from these regions can be detected as a narrow Ly α emission in the DLA trough (Hennawi et al. 2009; Finley et al. 2013).

If the absorbing cloud gets denser, smaller, and closer to the quasar, then we expect the narrow emission line in the DLA trough to increase in strength. In extreme cases where the hydrogen density is very high (i.e. $n_{\text{H I}} > 1000 \, \text{cm}^{-3}$) and the cloud size is smaller than the size of the quasar broad-line region (BLR), the leaked broad Ly α emission

from the BLR can fill the DLA trough completely and the DLA absorption profile is therefore not seen in the spectrum (Fathivavsari et al. 2016). This is why these DLAs are called *ghostly*-DLAs. The characterization of this kind of systems is extremely important to understand the details of how the neutral gas ends up at this position in such a harsh environment.

Conversely, the fact that a cloud smaller than the typical BLR size only partially covers the emission can constrain the spatial structure of the emission. These systems are potentially a powerful tool to study the structure of the BLR.

The BLR is thought to be composed of approximately virialized gas in the vicinity of the black hole (Netzer 2008). From this idea, it is possible to derive the typical size of the emission by performing reverberation mapping analysis (Shen et al. 2019). These studies reveal an expected correlation between the BLR size and the central luminosity (Bentz et al. 2013). However, it is also possible that at least part of the broad emission lines are produced by outflowing material launched from near the accretion disc. This is most strikingly suggested by observations of broad absorption lines (BALs) in about 20 per cent of quasars and the link between the emission lines and BALs has been studied in details (Matthews et al. 2020). Observationally, reverberation mapping of the H β emission of quasars at low redshift has resulted in constraining the geometry and kinematics of the region emitting this line. Grier et al. (2017) found these emission regions to be thick discs that are close to face-on to the observer with kinematics that are well described by either elliptical orbits or inflowing gas. Time lags as a function of the velocity across the H β emission-line profile have been measured in a number of AGNs. Various kinematic signatures have been found in the different objects; these kinematic signatures are mostly virialized

⋆ E-mail: brivael.laloux@hotmail.fr (BL); ppetitje@iap.fr (PP)

motions and inflows but also outflows (Du et al. 2016; Hamann et al. 2018; Giustini & Proga 2019).

These studies have been complemented by analysis of microlensing amplification of quasar continua and emission lines. Microlensing-induced line profile deformations analysis can constrain the BLR size, geometry, and kinematics (Schneider & Wambsganss 1990). Comparisons with models reveal that strong microlensing effects put important constraints on the size of the BLR (Braibant et al. 2017). Comparisons with observations show that flattened geometries (Keplerian disc and equatorial wind) can more easily reproduce the observed line profile deformations than a biconical polar wind (Hutsemékers et al. 2019).

In this paper, we construct simple models of the BLR, partially covered by an absorbing cloud, and use these models to characterize and fit observations of quasar spectra bearing *ghostly*-DLAs. In these spectra, although a DLA cloud is present in front of the quasar, no Lyα trough is detected whereas a Lyβ trough, when redshifted in the observed wavelength window, is clearly seen. We use the fact that only part of the BLR is covered to investigate whether it will be possible to differentiate between models and to constrain some properties of the BLR and of the absorbing cloud. An important starting point of our models is that we require them to reproduce the typical spectrum of a bright high-redshift quasar represented by a quasar template.

We describe the models in Section 2, explore how the models can produce *ghostly*-DLAs in Section 3, investigate the use of the models by fitting mock spectra in Sections 4 and 5, fit real SDSS data in Section 6, and draw conclusions in Section 7.

2 MODELLING THE QUASAR SPECTRUM

In the following, we model the quasar spectrum in the Lyα and Lyβ emission regions. The quasar is described as a central point-like source emitting a power-law continuum surrounded by a BLR described as a distribution of clouds with particular spatial and kinematic structures (see below) and a more extended NLR. Each cloud of the BLR is supposed to emit the same amount of Lyα photons. The rest-frame emission of each cloud is modelled as a Gaussian emission line of width FWHM = 50 km s^{-1}. The stratification of the BLR is defined by the density of clouds through the structure. Transfer of Lyα photons is not considered, which means that we assume the covering factor of the BLR clouds to be small. The BLR emission line is the superposition of the individual emissions of the clouds after taking into account their velocities. We add a narrow emission line to the spectrum corresponding to the NLR emission. This region will be assumed not to be covered by the absorbing cloud. As described below, we will use three different geometrical models of the BLR: a spherical model, a wind model, and a Keplerian disc model.

The typical radius of the high-redshift quasar BLR is of the order of 1 pc. However, our models do not depend on the exact radius of the BLR and in the following, radial dimensions in the BLR or in the cloud will be defined as the unit free ratio $r \equiv r_0/r_{BLR}$, where r_0 is the real radial dimension and r_{BLR} is the BLR radius, both in pc units.

To adjust the parameters of the models, we fit their outputs to a composite quasar spectrum obtained using 2200 quasar spectra of the Sloan Digital Sky Survey (SDSS; Vanden Berk et al. 2001). Since we are interested in the quasar Lyα emission, we subtract the N V emission from the template. For this, we fit the composite spectrum with two sets of two Gaussians representing the Lyα and N V emissions. The widths of the Gaussian functions are the same for
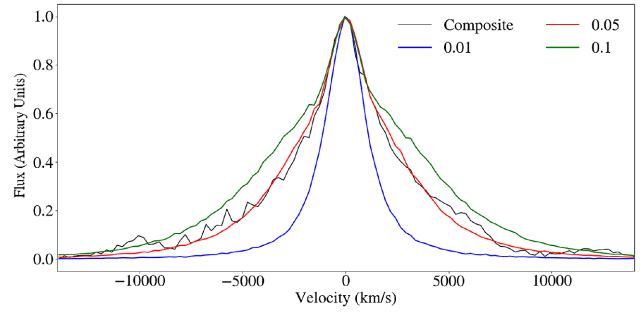

Figure 1. Comparison of spectra derived from the spherical model with the quasar composite spectrum after subtraction of the quasar continuum and the N V emission and represented by the black line. The blue, red and green curves correspond to $\sigma_0 = 9000$ km s^{-1} and $r_{min} = 0.01$, 0.05, and 0.1, respectively.

the two emissions. We then remove the contribution of the N V λ1240 emission line to obtain the typical Lyα quasar emission (represented by the black line on e.g. Fig. 1).

To model the spectrum of a *ghostly*-DLA, we will add an absorbing cloud on top of the continuum and the BLR emission, the NLR staying uncovered.

2.1 Spherical model

In this model, the distribution of point-like clouds around the quasar is spherical. The density of clouds depends on the distance to the centre r and is given by the following density profile:

$$n = n_0 \left(\frac{r}{r_{min}} \right)^{-\alpha}, \quad (1)$$

where n_0 is the number of emitting clouds at the internal radius r_{min}, the sphere being empty from $r = 0$ to r_{min}. We use $\alpha = 0.5$.

The velocity of each cloud relative to the observer is random and follows a Gaussian probability function of dispersion σ (Done & Krolik 1996). This dispersion depends on the distance to the centre and behaves according to Keplerian laws:

$$\sigma = \sigma_0 \left(\frac{r}{r_{min}} \right)^{-0.5}, \quad (2)$$

where σ_0 is the maximum dispersion.

To fill the BLR with clouds, the sphere is divided into 1100 layers in which emitting clouds are randomly distributed one by one until reaching the desired density in the layer. The first inner layer has 1100 clouds. The total number of clouds in the BLR is 356 400. These numbers are chosen so that the resulting spectrum is smooth enough keeping the computing time reasonable.

Given the above velocity law, it happens that amongst the two parameters that determine the width of the BLR Lyα emission, r_{min} and σ_0, r_{min} is the most important. In Fig. 2, we represent the Lyα emission of the BLR for three different values of r_{min} and σ_0.

In Fig. 1, we fit the composite spectrum (after subtraction of the quasar continuum) with a modelled quasar spectrum built from the addition of the BLR and NLR emissions.

We find that the spectrum is reasonably well reproduced with $0.03 \leq r_{min} \leq 0.05$ and $8500 \leq \sigma_0 \leq 10\,000$ km s^{-1}. The width of the NLR emission is in the range 400–700 km s^{-1}. For the rest of this paper, we will fix $r_{min} = 0.05$ and consider σ_0 and the width of the NLR as free parameters.
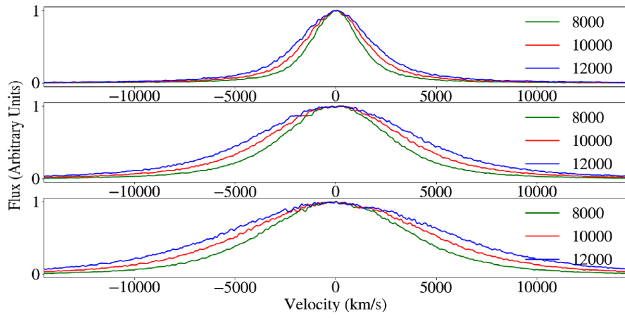
Figure 2. Modelled Ly α emission spectra of the spherical BLR model as a function of the maximum standard deviation (8000, 10 000, and 12 000 km s^{-1} for the green, red, and blue curves, respectively) for different inner radius, $r_{\min} = 0.01$, 0.05, and 0.1, for the top to bottom panels, respectively.
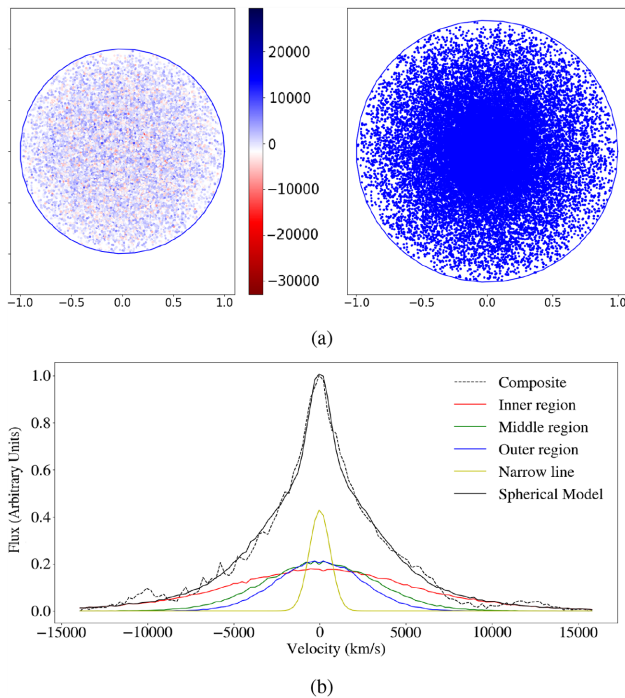

Figure 3. Layout of the spherical BLR model (panel a) and its corresponding spectrum (panel b). In the top left-hand panel, the colour scale corresponds to the velocity (in km s^{-1}) of the clouds relative to the observer. In the right-hand panel, the blue dots illustrate the variation of the density of clouds in the BLR. In panel (b), the composite quasar spectrum is fitted with the spherical model with $\sigma_0 = 10\,000$ km s^{-1}, a BLR/NLR strength ratio of 2.33 and the width of the narrow line of 500 km s^{-1}. The contributions of different regions of the BLR (inner for $0 < r < 0.33$, middle for $0.33 < r < 0.66$, and outer for $0.66 < r < 1$) are singled out and shown as red, green, and blue lines respectively.

The spatial layout of the emitting clouds in the BLR and the corresponding spectrum for the spherical model are shown in Figs 3(a) and (b), respectively. The dots are coloured according to their velocity relative to the observer in the left-hand panel. In the right-hand panel, the dots are plotted with the same colour to better illustrate the variation of the density within the BLR.

We then single out three regions as a function of their distance to the centre, the inner region from the centre to $r = 0.33$, the intermediate region from $r = 0.33$ to 0.66, and the outer region from $r = 0.66$ to 1. Their respective contributions to the spectrum are

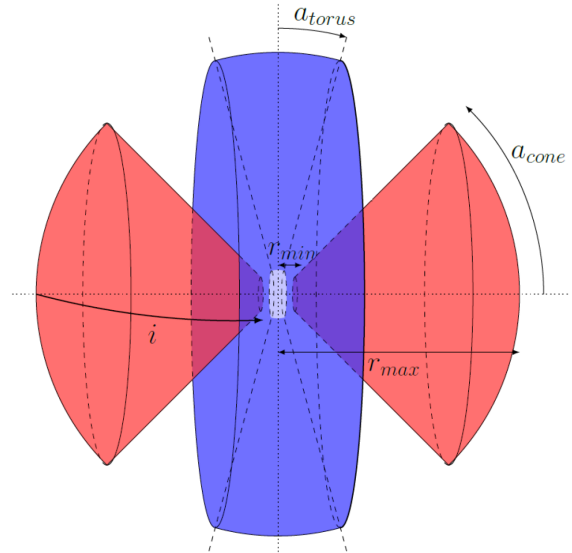**Figure 4.** Sketch of the wind model with an inclination of the model axis relative to the line of sight to the observer, $i \sim 85°$. In red, the polar wind with an opening angle $a_{\text{cone}} = 45°$. In blue, the equatorial wind with an angle $a_{\text{torus}} = 15°$. Both winds have an internal radius $r_{\min} = 0.1$ and an external radius $r_{\max} = 1$.

represented in Fig. 3(b) by a red, green, and blue line, respectively. Dots located near the centre have a larger dispersion in velocities (see equation 2) than the one located further away, this is why the wings of the spectrum are only produced by the emitting clouds located in the centre.

2.2 Wind model

The second model is a combination of two models described in Braibant et al. (2017). We associate two winds, one equatorial and one polar (see Fig. 4). The velocity and density of the point-like clouds within the wind are described below.

As shown in blue in Fig. 4, the equatorial wind is a torus with an angle $a_{\text{torus}} = 15°$ as in Braibant et al. (2017). In red, the polar wind is composed of two opposite cones with an opening angle $a_{\text{cone}} = 45°$. The later value is a compromise. Indeed, a smaller value would result in a gap on top of the emission line, when a larger value would mingle the contributions of the two winds implying a result close to the spherical distribution. The cone and the torus are coaxial. The outer limit of both winds are $r_{\max} = 1$ as for the spherical model but the inner radius is fixed at $r_{\min} = 0.1$. The spectrum is much less sensitive to the later parameter as compared to the spherical model.

The point-like clouds in the wind flows have a radial velocity relative to the centre given by the following law:

$$v(r) = v_{\max} \ln \left(1 + \frac{r}{r_{\max}}(e^1 - 1) \right). \tag{3}$$

$v_{\max}$ is the maximal velocity of these clouds, reached at the maximal considered distance $r_{\max} = 1$. Since the AGN winds are radiative pressure driven, the clouds are accelerating outwards. The acceleration should decrease with the distance. This is why we chose a logarithmic velocity law for which the velocity is null at $r = 0$ and which reproduces better the shape of the quasar Ly α emission. The ad hoc factor $(e^1 - 1)$ was added only to fulfill the condition $v(r = r_{\max}) = v_{\max}$.
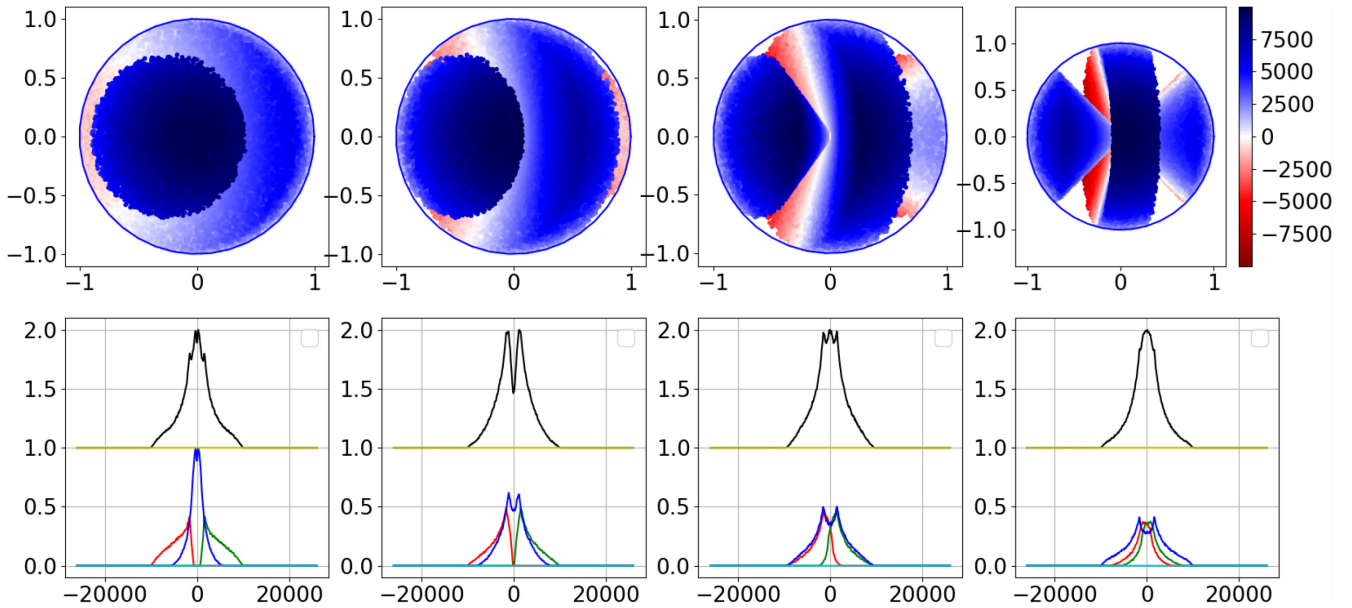
Figure 5. In the first row, the layouts of the wind model BLR are represented for different inclinations: $i = 20°, 40°, 60°$, and $80°$. Their respective spectra, with no NLR emission added, are shown in the second row. The colour of the dots representing the emitting clouds are scaled as shown on the right-hand side of the top panels. The total spectrum (black line, middle row) is the sum of three contributions from the torus (blue line), the front cone (red line), and the back cone (green line) shown in the bottom row.

The emitting clouds are not homogeneously spread inside the winds. The density of clouds is obtained by imposing the flux of clouds crossing the boundary of the layers to be conserved through the wind flow. We use 750 layers and the first of them has 750 clouds in it, for a total of 350 252 emitting clouds inside the BLR. The number of layers and the number of clouds inside the first one are chosen such as the resulting spectrum is smooth and the wind model has a similar total number of clouds as the spherical one.

We then construct the observed spectrum by defining the observer position relative to the model axis. In this model, it must be noted that we only need one angle that is the inclination, i, of the axis relative to the line of sight to the observer. Indeed, by axial symmetry, all other positions will be recovered by a simple rotation.

Due to its peculiar geometry, the spectrum produced by the wind model varies as a function of the inclination, i, of the BLR. Fig. 5 shows the spatial layout of the BLR and its corresponding spectrum for four values of the inclination : $i = 20°, 40°, 60°$, and $80°$. In the same way as for the spherical model, the colour of the dots indicates their velocity relative to the observer. However, due to the representation, it should be reminded that when projected in the same region of the sky, the blueshifted dots are hiding the redshifted ones, and thus for instance a DLA cloud located in the centre of a BLR with $i = 20°$ will not only obscure the blueshifted contribution but also the redshifted one not represented here. We have not added an NLR emission here to have a better insight on the contribution of each part of the BLR.

At low inclination angle, the absolute projected velocity of the clouds in the torus are small and accordingly the torus contribution is a narrow component centred at zero velocity whereas the contributions by the cones are spread at higher velocities and are well separated. When the inclination increases, the contribution by the torus is more spread over the velocities and is mixed with the contributions by the cones.

As an example, we show in Fig. 6 that we can reproduce the composite spectrum with typical parameters: $i = 60°$, $v_{max} =$
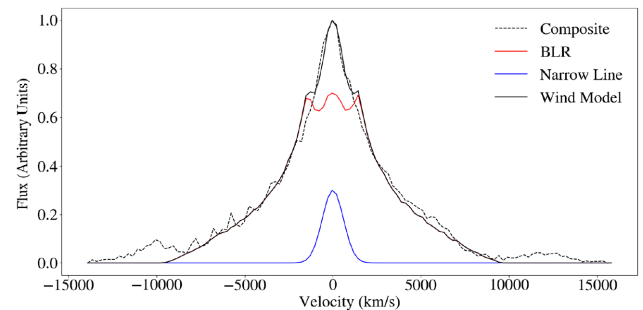

Figure 6. Comparison of the composite spectrum (Vanden Berk et al. 2001) after subtraction of the quasar continuum and the N V emission (black dashed line) with a spectrum obtained with the wind model (see the text). The model (black solid line) is the sum of the BLR and NLR contributions (red and blue solid lines, respectively).

9500 km s^{-1}, the width of the narrow line is 500 km s^{-1}, and the BLR/NLR strength ratio is 2.33.

2.3 Keplerian disc model

We use a simplified version of the model described in Pancoast, Brewer & Treu (2014) and favoured by interferometric observations (Gravity Collaboration et al. 2018). The model consists of a thick disc with half-opening angle $\theta_0 = 45°$ in which point-like emitting clouds are moving along circular orbits around the black hole (see Fig. 7). The emitting clouds are assigned a distance to the centre with the following distribution:

$$r = r_{min} + g\left(\frac{1}{\beta^2}\right) \times (1 - F)\beta^2 \, r_{BLR},   \quad (4)$$

where $g\left(1/\beta^2\right)$ is a gamma distribution with a shape parameter $\beta = 1.4$ and $F = r_{min}/r_{BLR}$ with $r_{min} = 0.1$ and where r_{BLR} is the mean
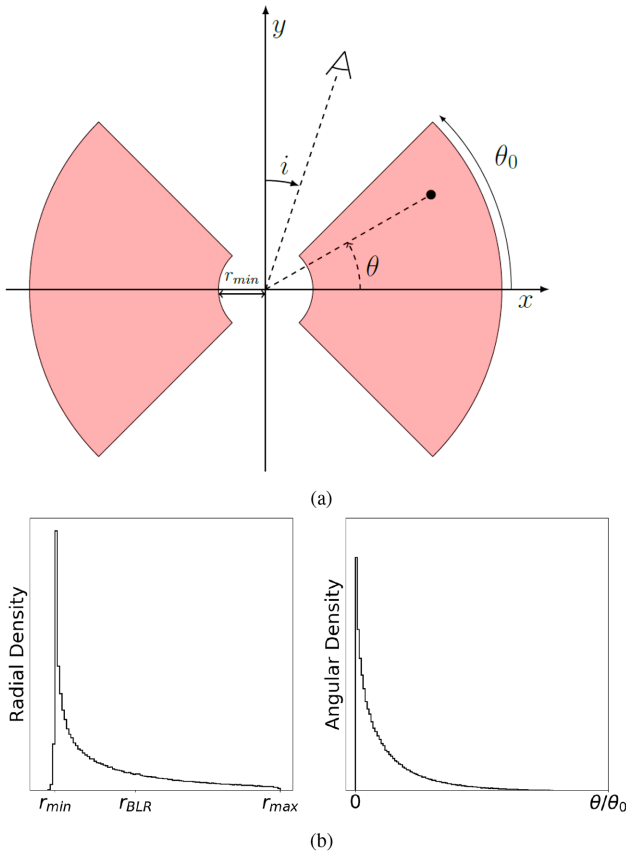
(a)

(b)

Figure 7. Top panel: sketch of the cut view of the Keplerian disc model. The opening angle of the disc is $\theta_0 = 45°$. Bottom panels: radial (left-hand panel) and angular (right-hand panel) cloud density probabilities.

radius of the BLR. We use the dimensions of the model by Gravity Collaboration et al. (2018) so that $r_{BLR} = 0.42$. As for other models, the maximum radius of the BLR is $r_{max} = 1$.

The azimuth θ of the clouds follows an exponential probability distribution of scale height $\theta_0/4$ as presented in Fig. 7(b).

The velocity of the clouds is given by

$$v(r) = v_0 \times \sqrt{\frac{r_{\min}}{r}}, \qquad (5)$$

with v_0 being a free parameter. The direction of the velocity is perpendicular to the radius of the orbit. The total number of clouds in the BLR is 350 000 such as it matches with the previous two other models.

As it can be seen on the right-hand panel of Fig. 8, blueshifted clouds are located on one side of the plane when redshifted clouds are located on the other side.

The left-hand panel of Fig. 8 shows the fit of the quasar template with this model. It can be seen on the figure that the BLR spectrum shows two peaks widely separated implying that the needed NLR emission has a broader width, FWHM = 900 km s^{-1} in this case. The main parameter of the model is the inclination, i, between the disc axis and the line of sight to the observer.

3 GHOSTLY DLAS

A *ghostly*-DLA is the result of the presence of a small absorbing cloud in front of the BLR. The cloud is small enough so that part of the BLR is not covered. One very important observational fact to bear
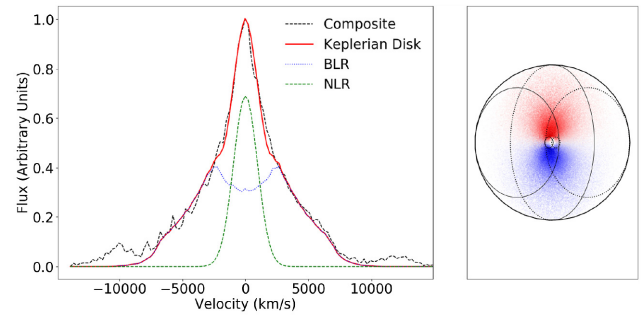

Figure 8. Left-hand panel: fit of the quasar composite spectrum by the Keplerian disc model. The quasar continuum and the N v emission have been subtracted beforehand. Total, BLR, and NLR spectra are represented by red, blue, and green curves, respectively. Right-hand panel: The relative projected velocities of the emitting clouds are represented by dots with colours indicating their direction. The inclination of the disc is $i = 40°$. To ease the visualization, the edges of the disc are represented by full lines when they are on the side of the observer and dotted lines when they are hidden on the opposite side.

in mind is that the cloud must cover the central source of continuum. Indeed, *ghostly*-DLAs are identified by the presence of strong metal absorption lines some of them being redshifted in spectral regions devoid of any emission line.

After placing the DLA-cloud in front of the BLR, we define which emitting clouds are covered and which are not. We derive the total emission of the covered region and apply to the resulting spectrum the absorption by the amount of neutral hydrogen in the cloud. We then add to the absorbed spectrum the contribution of the uncovered part of the BLR.

For simplicity, we consider a cylindrical absorbing cloud of radius r_{cloud} and constant column density. The resulting spectrum depends on several characteristics of the absorbing cloud: its column density (which can be estimated from the Lyman series absorptions when these lines are seen in the quasar spectrum), its position, its size; but it depends also on the inclination of the BLR with respect to the observer in the case of the wind and disc models.

In the following, we illustrate the impact of an absorbing cloud on the modelled quasar spectra. We impose the BLR models to reproduce the template quasar emission and therefore fix parameters so that models do so (see the previous section).

For this exercise, we assume that the quasar continuum has the same density flux as the top of the Ly α emission line that is typical of bright quasars at these redshifts and that the column density of the absorbing cloud is log N(H I)(cm^{-2}) = 21. In addition, we intentionally minimize the flux from the NLR component to illustrate better the consequences of partial coverage of the BLR. In the two following subsections, we do not add any NLR emission.

3.1 Position of the cloud

Given the symmetries of the models, the position of the absorbing cloud has more impact on the resulting spectrum for the wind and disc models.

In the left panel of Fig. 9, we present spectra obtained with the wind model assuming an absorbing cloud located at the different positions indicated in the right panel. The inclination of the cone is 60° and the cloud has a radius $r_{cloud} = 0.4$. The unabsorbed quasar spectrum is shown as the dotted black line and the green line represents the spectrum of the quasar with the cloud centred at $(-0.6, 0)$, thus not
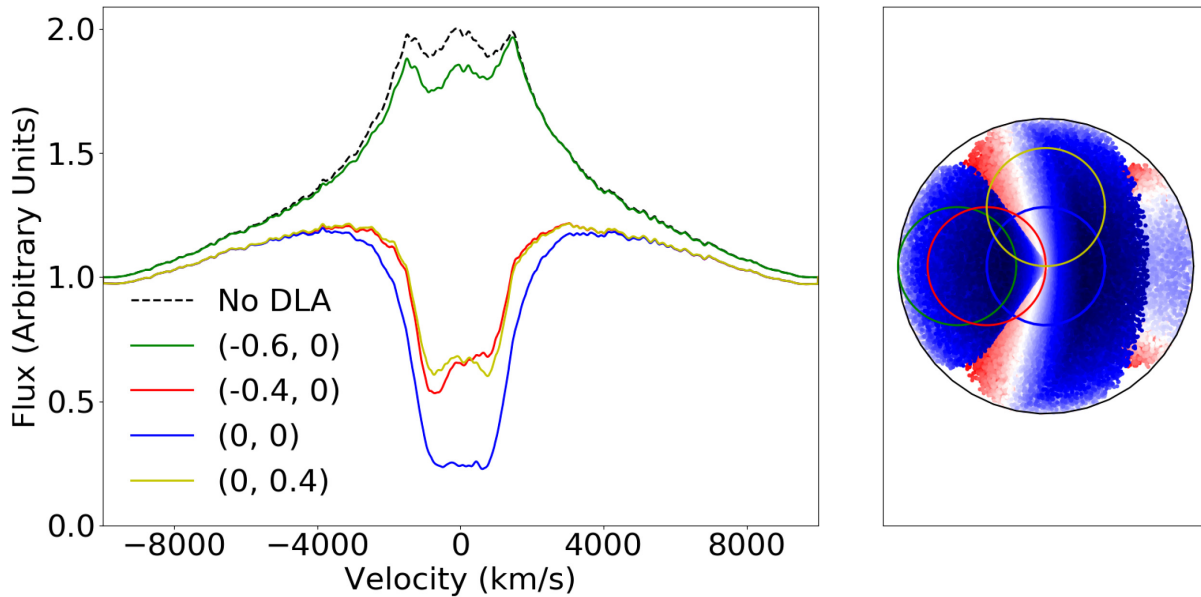
Figure 9. The left panel shows spectra built with the wind model (with $i = 60°$) and an absorbing cloud located at different positions as indicated in the right panel. The absorbing cloud has a column density $\log N(\text{H\,I})(\text{cm}^{-2}) = 21$ and a radius $r_{\text{cloud}} = 0.4$. The quasar spectrum without any absorption and with no NLR emission is represented with a dotted black line.

covering the source of continuum located in the centre. The other positions of the cloud are at $(-0.4, 0)$ (red solid line), $(0,0)$ (blue solid line), and $(0,0.4)$ (yellow solid line). Note that, by symmetry, the spectrum will be the same if the cloud is centred at $(0, -0.4)$ or at $(0,0.4)$. For the same reason, when the cloud is at $(0.4,0)$ the spectrum will be the mirror version (relative to the zero velocity) of the spectrum when the cloud is at $(-0.4, 0)$. Indeed, the covered BLR-emitting clouds moving toward the observer in one case are moving away in the other case. One can notice that the absorption is more important when the cloud is centred at $(0,0)$. This is due to the higher density of emitting clouds at small distances from the centre. Only a small fraction of these numerous low-velocity-emitting BLR clouds are covered by the absorbing cloud when located far from the centre. One can also notice the asymmetry in the $(-0.4, 0)$ spectrum due to the majority of emitting clouds with negative velocity covered, whereas the $(0,0.4)$ spectrum is symmetric due to the same number of emitting clouds with negative and positive velocities covered. One can argue none the less that the difference between the two cases is rather small, but in other situations, the difference could be more significant.

In the left panel of Fig. 10, we present the spectra obtained with the disc model assuming an absorbing cloud located at the different positions indicated in the right panel, which are identical to those used for the wind model. The spectra look similar to that of the wind model but with a symmetry relative to the *y*-axis instead of a symmetry relative to the *x*-axis. It is apparent however that, because of the large opening angle of the disc, the red and blue peaks in the corresponding quasar spectrum are less absorbed resulting in the wings of the absorption trough to be steeper. The resulting two emission peaks on both sides of the absorption are more distant compared to the wind model. This implies that the NLR emission, needed to fill the residual absorption, will have to be broader for these models than for the wind model. This could imply that for a fixed radius the absorbing cloud should be closer to the AGN in order to avoid absorption of the central part of the NLR where velocities are expected to be larger.

3.2 Size of the cloud

Fig. 11 shows how the spectrum evolves with the size of an absorbing cloud centred at $(0,0)$ for the three models, the spherical model (upper panel), the wind model (middle panel), and the disc model (bottom panel).

The continuum and the BLR flux levels have been fixed to 1 and the absorbing cloud column density is still $\log N(\text{H\,I}) = 21.0$. For the wind and disc models, the inclination of the model axis is $60°$ and $40°$, respectively. As one could expect, the absorption is getting more prominent when the size of the absorbing cloud increases. One can see that it is easy to reproduce a *ghostly*-DLA for the spherical and wind models without tuning the parameters. It is possible to hide the absorption even more by decreasing the ratio between the continuum and the BLR fluxes. This is obtained without adding an NLR emission that is not absorbed and would fill in part if not all of the residual absorption. To obtain a *ghostly*-DLA with the disc model is more difficult and a stronger NLR is needed.

3.3 Examples

With the models, we can tune the parameters to obtain spectra of different types of quasar Lyα emission lines. As said before and derived from observations, we impose the cloud to cover the quasar source of continuum. We also add a weak NLR emission. In Figs 12–14 for the spherical, wind, and disc models, respectively, we show the spectrum of a quasar with no absorption (upper right panel), and the same with an absorbing cloud in front (two other panels). The corresponding spatial structure is shown in the left-hand panels. It can be seen that the spectra in the middle panels correspond to an eclipsing DLA, where the absorbing cloud behaves as a coronagraph and only a weak narrow Lyα emission is seen in the bottom of the trough (Finley et al. 2013). The spectra in the bottom panels correspond to *ghostly*-DLAs. To obtain an eclipsing DLA-QSO in the case of the spherical and disc models, the radius of the absorbing cloud must be large enough to cover a significant portion of the
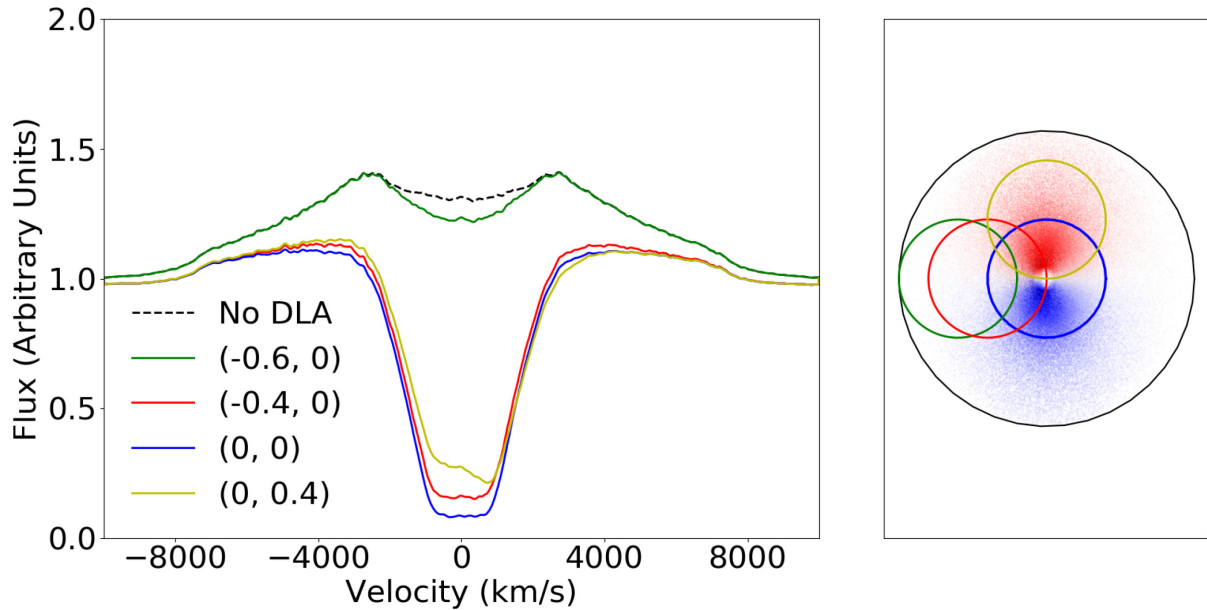
Figure 10. The left panel shows spectra built with the disc model (with $i = 40°$) and an absorbing cloud located at different positions as indicated in the right panel. The absorbing cloud has a column density log $N(\mathrm{H\,I})(\mathrm{cm}^{-2}) = 21$ and a radius $r_{\mathrm{cloud}} = 0.4$. The quasar spectrum without any absorption and with no NLR emission is represented with a dotted black line.
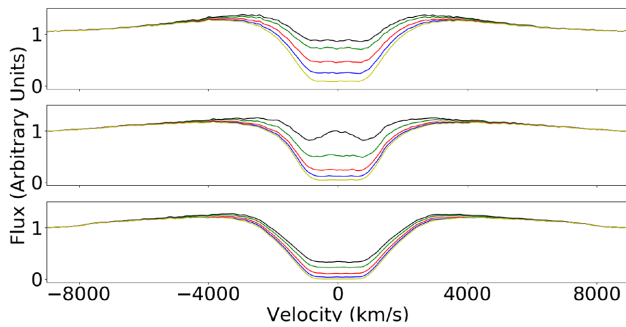
Figure 11. Spectra obtained with the spherical model (upper panel), the wind model (middle panel), and the Keplerian disc model (lower panel) with an absorption cloud located at (0,0) and with a radius of 0.1 (black line), 0.2 (green line), 0.4 (red line), 0.6 (blue line), and 0.8 (yellow line).

BLR. Whereas the cloud can be smaller in the case of the wind model geometry.

On the other hand, to obtain a *ghostly*-DLA, the absorbing cloud must be rather small so that the non-covered emission fills up at least part of the absorption. A high BLR flux relative to the continuum flux also helps to obtain such *ghostly*-QSOs. More importantly, a strong NLR emission can fill in the trough as soon as the width of the DLA absorption trough matches the width of the NLR emission.

The evolution of the models as a function of the different parameters is discussed in more details in the next section.

4 INVESTIGATION OF THE MODELS

Our main objective is to extract any information on the BLR structure and on the characteristics of the absorbing cloud from observations of *ghostly*-DLA QSOs by comparing the quasar spectra with the outputs of our models. Before performing direct comparison, we would like

to gain insight on which parameters can be constrained best. To do so, we will construct realistic mock spectra and fit them back with our models.

4.1 Mock spectra

Mock spectra are built from the models described earlier. We impose parameters so that the modelled emission spectrum fits the quasar composite spectrum. We then choose the parameters of the absorbing cloud: its size, position, and column density, in such a way that the corresponding spectrum belongs to the *ghostly*-DLA category. An important characteristic of these spectra is that the source of the quasar continuum located at the centre of the models must be covered by the absorbing cloud. Indeed, strong metal lines are observed associated with *ghostly*-DLAs some of them redshifted in wavelength ranges devoid of emission lines.

Noise is added to the modelled spectrum with a given signal-to-noise ratio (S/N) and the spectrum is rebinned to a spectral resolution R. For each model, we will consider spectra with $R = 2500$ and S/N $= 10$ on the one hand and $R = 5000$ and S/N $= 50$ on the other. The first case (LR for low resolution) corresponds roughly to the characteristics of good SDSS spectra. The second case (HR for high resolution) investigates what could be done with better data that could be obtained with e.g. XSHOOTER on the VLT. Given the width of the lines, higher spectral resolution is not needed.

The chosen parameters for the models are presented in the first row of Tables 1–3 for the spherical, wind, and disc models, respectively.

4.2 Fit of mock spectra

Once a mock spectrum has been generated, it is fitted with the three models in order to estimate the degeneracy between models and to evaluate our capability to recover some of the true parameters. For this, we compute the reduced χ^2 between the mock spectrum and

Table 1. Results from the fit of a mock spectrum constructed with the spherical model in two versions LR and HR.

No.	Method	Quality	N(H I)	Radius	x coordinate	y coordinate	Inclination	Strength NLR	Strength BLR	χ^2
1	Spherical	NA	20.6	0.3	0.0	0.0	NA	0.60	1.40	NA
2	Spherical	LR	**20.6**	0.4	0.24	**0.0**	NA	**0.59**	**1.40**	1.01
3	Spherical	HR	**20.6**	0.5	0.12	**0.0**	NA	**0.66**	**1.39**	1.13
4	Wind	LR	21.0	0.2	**0.0**	0.18	50	0.29	1.89	1.03
5	Wind	HR	21.0	0.1	**0.0**	**0.0**	50	0.01	1.81	2.11
6	Disc	LR	20.3	0.2	0.04	− 0.02	30	0.88	0.90	1.06
7	Disc	HR	20.3	0.1	0.07	− 0.07	30	0.79	0.91	3.52
8	Wind	LR	**20.6**[a]	0.9	0.09	0.81	50	0.86	1.58	1.11
9	Wind	HR	**20.6**[a]	0.8	0.0	0.72	50	0.93	1.57	4.12
10	Disc	LR	**20.6**[a]	0.9	0.09	0.18	0	1.11	5.37	1.13
11	Disc	HR	**20.6**[a]	0.2	0.18	− 0.04	20	0.68	1.18	4.72

Notes. The input parameters are indicated in the first row. We fit the low- and high-resolution spectra with the spherical, wind, and disc models to try to recover the input parameters. The parameters of the best fits for the different models are presented in rows 2–7. When the fit recovers the initial parameter within 10 per cent, the value is printed in boldface. [a]The second part of the table (rows 8–11) shows the same with the neutral hydrogen column density fixed at the correct value (20.6) as indicated by an "a".

Table 2. Results from the fit of a mock spectrum constructed with the wind model in two versions LR and HR.

No.	Method	Quality	N(H I)	Radius	x coordinate	y coordinate	Inclination	Strength NLR	Strength BLR	χ^2
1	Wind	NA	20.3	0.4	0.16	0.32	60	0.6	1.4	NA
2	Wind	LR	**20.3**	**0.4**	0.08	0.36	50	0.80	1.31	0.86
3	Wind	HR	**20.3**	0.6	0.60	0.0	**60**	**0.56**	**1.40**	1.11
4	Spherical	LR	**20.3**	0.3	0.30	0.0	NA	**0.57**	1.16	1.08
5	Spherical	HR	**20.3**	0.1	0.1	0.0	NA	0.37	1.17	5.22
6	Disc	LR	**20.3**	0.6	0.0	− 0.30	0	**0.57**	4.25	0.97
7	Disc	HR	**20.3**	0.7	0.07	− 0.56	0	0.0	4.28	3.82

Notes. The input parameters are indicated in the first row. We fit the low- and high-resolution spectra with the spherical, wind and disc models to try to recover the input parameters. The parameters of the best fits for the different models are presented in rows 2–7. When the fit recovers the initial parameter within 10 per cent, the value is printed in boldface.
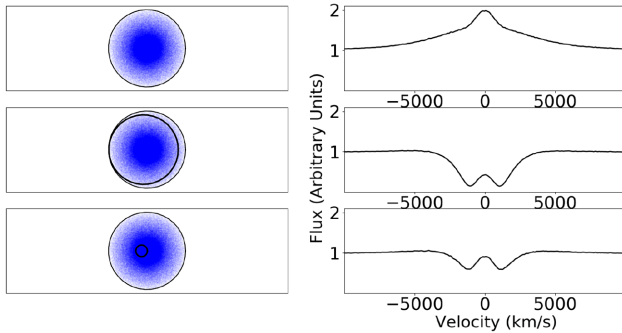
Figure 12. Examples of spherical model spectra (right-hand column) and their corresponding spatial structure (left-hand column). From the top to bottom: regular QSO, eclipsing DLA QSO, *ghostly*-DLA QSO.
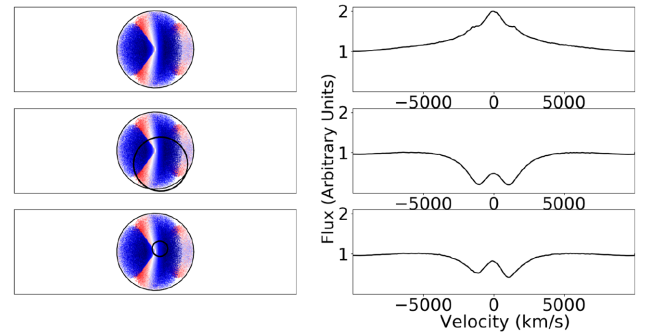
Figure 13. Examples of wind model spectra (right-hand column) and their corresponding spatial structure (left-hand column). From the top to bottom: regular QSO, eclipsing DLA QSO, *ghostly*-DLA QSO.

the models built with every possible parameter combination. The reduced χ^2 is computed as follows:

$$\chi^2 = \frac{1}{n-m} \sum_i \frac{(O_i - M_i)^2}{\sigma_i^2}, \tag{6}$$

where n is the number of pixels, m the number of fitted parameters, O_i the observation, M_i the model, and σ_i^2 the variance of

the data. As the far wings of the emission are not well reproduced by our simplified models, the χ^2 computation is performed taking into account only the pixels between −7000 and +7000 km s^{-1}.

We vary the parameters as follows:

(i) The radius of the absorbing cloud: every tenth of a distance unit from 0.1 to 0.9.
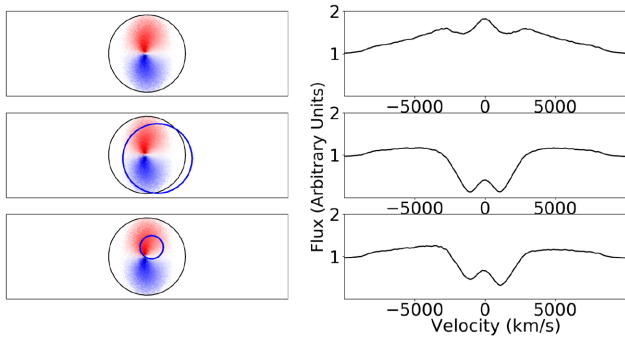
Figure 14. Examples of Keplerian disc model spectra (right-hand column) and their corresponding spatial structure (left-hand column). From the top to bottom: regular QSO, eclipsing DLA QSO, *ghostly*-DLA QSO.

(ii) The x coordinate of the quasar: every tenth of the radius of the cloud, going from 0 to r_{cloud} for the spherical and disc models and from $-r_{cloud}$ to r_{cloud} for the wind model.

(iii) For the wind and disc models, the y coordinate: every tenth of the radius of the cloud such as $\sqrt{x^2 + y^2} < r_{cloud}$. For the wind model, $y \geq 0$, whereas it can be positive or negative for the disc model.

(iv) For the wind and disc models, the inclination of the BLR: every 10°, from 0° to 90°.

(v) The column density: 12 values between $\log N(\text{H\,I}) = 19.0$ and 21.4.

(vi) The strengths of the NLR and BLR emissions are varied only slightly to optimize the fit.

Note that we fix the width of the NLR to $\text{FWHM}_{NLR} = 600 \text{ km s}^{-1}$ and the maximal velocity $v_{max} = 10\,000 \text{ km s}^{-1}$ for the spherical and wind models. For the disc model, the width of the NLR component is also fixed but at $\text{FWHM}_{NLR} = 950 \text{ km s}^{-1}$.

We vary the free parameters and compare the mock spectra with hundred of thousands of models. In reality, note that the column density for some *ghostly*-DLAs with high enough redshift could be inferred from the Lyman series. We however want to check if our method can recover the correct column density in case these lines are not available in the observed wavelength window.

4.3 Spherical model

Parameters from which we construct the mock spectrum of the spherical model are listed in the first row of Table 1. Since the BLR is a sphere, no inclination is needed but also, due to axial symmetry, the cloud is only moved along the *x*-axis, and the *y* coordinate is kept equal to 0.

We then fit the mock spectrum in its two versions, LR and HR, with the spherical, wind, and disc models. Results of the best fits are given in Table 1 from row 2 to 7.

The fits of the LR spectrum are equally good for all models due to the noise hiding the differences between the models. On the other hand, not surprisingly, the spherical model gives the best fit in HR. This is encouraging because this exercise shows that we may be able to distinguish between the three models providing good data with sufficiently high spectral resolution and S/N are available.

When the redshift of the system is high enough, the absorptions from the other Lyman series lines are seen in the quasar spectrum (Fathivavsari et al. 2016) and the neutral column density can be derived directly from these absorptions. We have therefore fixed the column density to the correct value and reproduce the exercise. The results are presented in Table 1 from row 8 to 11. We can notice higher χ^2 values for the wind and disc models, which makes the spherical model even more distinguishable from the other two models.

The ratio between BLR and NLR emissions is approximately retrieved. This is however not the case for the size of the DLA-cloud and its position even for the spherical model in HR. We will discuss further in the next section the constraints derived on the parameters.

Figs 15(a) and (b) show the mock spectrum (black line) in LR and HR versions, respectively, along with the best fit for all models. It can be seen that at low resolution and low S/N, it is not possible to discriminate between the three models. However, differences appear at higher resolution and S/N. The disc model fails to reproduce the shape of the trough. On the other hand, one can see that the wind model can reproduce the overall shape of the emission but fails to reproduce the far wings of the line and the two peaks of the emission differ slightly from the spherical ones. Note that the far wings are not taken into account in the fit as they may be a poor discriminant because of the simplicity of our models. In contrast, the differences seen in the shape of the peaks could be a good indicator to look at in real data providing the quality of the data is high enough.

4.4 Wind model

We construct a mock spectrum using the wind model, the input parameters of which are given in the first row of Table 2.

We then fit the mock spectrum in its two versions, LR and HR, with the spherical, wind, and disc models. Results of the best fits are given in rows 2–7 of Table 2. From the χ^2 values given in the table, it is clear that we cannot discriminate between the different models in LR. But, and as for the spherical model, we can do so if high-quality (HR) data are available.

An important fact is that independently of the resolution or of the model, the correct H I column density is recovered. However, this is not the case for the other parameters except the inclination and the BLR to NLR emission ratio for the wind model in HR.

Figs 16(a) and (b) show the mock spectrum (black line) in LR and HR versions, respectively, along with the best fit for the three models. Again, at low resolution and low S/N, it is difficult to discriminate between the models even though the spherical model (red line) seems to show too flat peaks. This impression is confirmed in HR. We observe in Fig. 16(b) that the flatness of the peaks of the spherical model does not allow this model to fit the mock spectrum well. We can also notice that the absorption feature of the mock spectrum is asymmetric that cannot be reproduced by the spherical model. Indeed, this asymmetry is the result of the spatial structure of the BLR in the wind model. For the spherical model, the absorption is bound to be symmetric as every cloud has the same probability to have a positive or negative velocity. In other words, negative and positive velocities are absorbed in the same way independently of the position or the size of the absorbing cloud.

The disc model spectrum shows peaks with a flatness intermediate between that of the spherical and wind models. The largest difference between the disc model and the mock spectrum, although not prominent, resides in the shape of the central part of the absorption trough, which is due to the peculiar inclination of the disc.

As Table 2 shows, the best inclination is 0°, which means that the mean plane of the disc is perpendicular to the line of sight.

Table 3. Results from the fit of a mock spectrum constructed with the disc model in two versions LR and HR.

No.	Method	Quality	N(H I)	Radius	x coordinate	y coordinate	Inclination	Strength NLR	Strength BLR	χ^2
1	Disc	NA	21.0	0.4	0.08	-0.32	40	0.69	0.41	NA
2	Disc	LR	**21.0**	**0.4**	0.0	-0.40	**40**	0.61	**0.37**	0.82
3	Disc	HR	**21.0**	**0.4**	**0.08**	**-0.32**	**40**	**0.69**	**0.41**	1.26
4	Spherical	LR	21.2	**0.4**	0.12	0.0	NA	0.44	0.86	1.06
5	Spherical	HR	**21.0**	0.9	0.0	0.0	NA	0.83	0.70	5.67
6	Wind	LR	21.2	0.7	-0.28	0.56	60	0.38	1.04	0.90
7	Wind	HR	21.2	0.9	-0.72	0.09	70	0.52	1.40	2.58

Notes. The input parameters are indicated in the first row. We fit the low- and high-resolution spectra with the spherical, wind and disc models to try to recover the input parameters. The parameters of the best fits for the different models are presented in rows 2–7. When the fit recovers the initial parameter within 10 per cent, the value is printed in boldface.
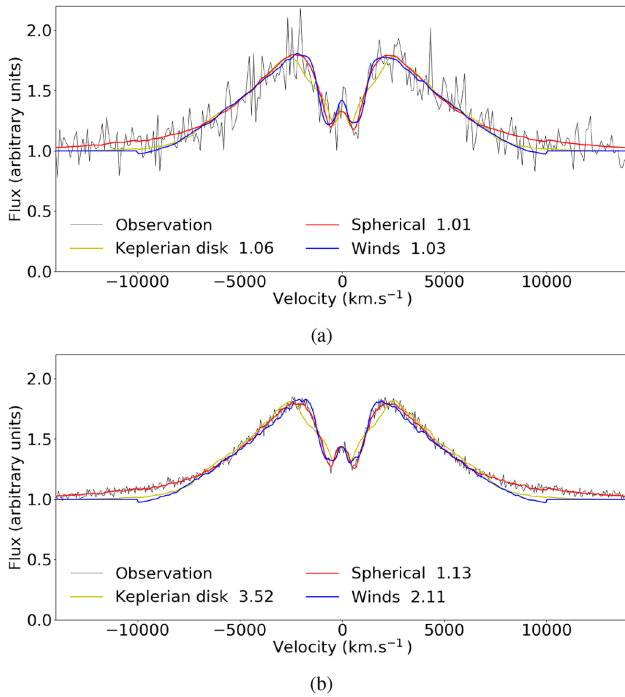
Figure 15. A mock spectrum (black line) is constructed with the spherical model in two versions, LR (panel a) and HR (panel b). Best-fitting models using the spherical model (red line), the wind model (blue line), and the disc model (yellow line) are overplotted. Note that far wings of the BLR emission are not considered in the fit.

4.5 Keplerian disc model

As we did previously, we construct a mock spectrum with the Keplerian disc model whose input parameters are displayed in the first row of Table 3. The best fit parameters for each model in LR and HR are presented in rows 2–7. The resulting χ^2 values indicate that the fits in LR are good for all three models. These fits are significantly worse in HR for the spherical and wind models, whereas the fit is good for the disc model, as expected. Once again we can recognize the model used to built the mock spectrum providing good spectral resolution and S/N are used for the observations.

We notice that the column density is pretty well recovered for all models. Besides, in HR, the fit using the disc model retrieves all the input parameters including the BLR to NLR flux ratio, together with the size and position of the absorbing cloud that is promising.
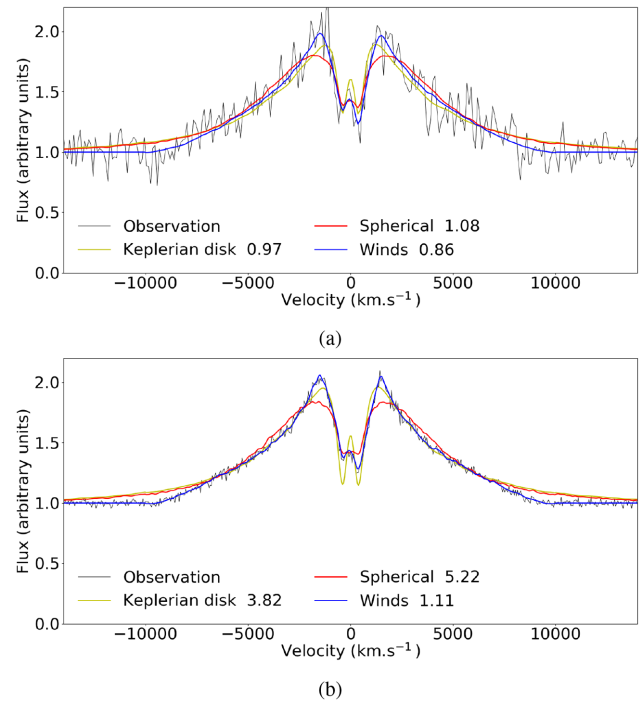

Figure 16. A mock spectrum (black line) is constructed with the wind model in two versions, LR (panel a) and HR (panel b). Best-fitting models using the spherical model (red line), the wind model (blue line), and the disc model (yellow line) are overplotted. The far wings of the emission are not taken into account in the fit.

In Figs 17(a) and (b), we display the mock spectrum together with the best fits using the three models. We can see that even in LR, the spherical model struggles to fit the mock spectrum properly as it fails to reproduce the asymmetry of the trough. This is even more apparent in HR. On the other hand, the wind model succeeds to reproduce the overall shape of the line in LR and even in HR except for some minor features.

4.6 Summary

From this study, we find that the model used to produce the mock spectrum can be recovered for the three models. However, this is valid only if the spectral resolution and the S/N are sufficient, meaning that with the quality of SDSS data, the distinction will be difficult. With higher quality data, some specific features can be
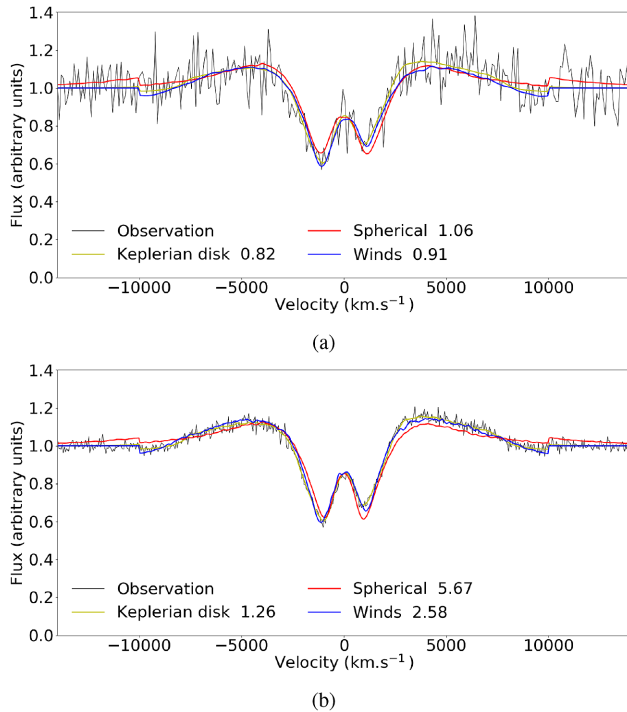
Figure 17. A mock spectrum (black line) is constructed with the Keplerian disc model in two versions, LR (panel a) and HR (panel b). Best-fitting models using the spherical model (red line), the wind model (blue line), and the disc model (yellow line) are overplotted. Note that the far wings of the emission are not taken into account in the fit.

used to discriminate between models such as the asymmetry of the trough rejecting automatically the spherical model. The flatness of the spherical model peaks is also a good indicator. In general, the wind and disc models are more versatile and are more difficult to disentangle.

An important result is that even with LR data, we can derive a good estimate of the H I column density. This will be investigated in more details in the next section.

5 INVESTIGATIONS OF THE PARAMETERS

We have shown in the previous section that we can reproduce ghostly-DLAs well and that there is a promising difference between models. In this section, we will try to understand if, *once a model is preferred*, we can derive quantitative constraints on parameters such as the inclination of the BLR in the case of the wind and disc models and the size, position and column density of the absorbing cloud.

To estimate these constraints, we first fix a reduced χ^2 threshold value to define an acceptable fit. Even though a χ^2 closer to 1 is considered better, a rule of thumb states that a value below 1.5 indicates an acceptable fit. It does not mean that a fit above this limit is bad. It only gives us a way to compare χ^2 values between the different fits.

We use the same mock spectra built from the three models with parameters as given in the first row of Tables 1–3 and we fit the mock spectra with the best model as derived from the previous section.

In the following, we chose one input parameter, fix its value and vary all other parameters deriving the minimum χ^2. We finally vary the value of the chosen parameter and study the evolution of this minimum χ^2.
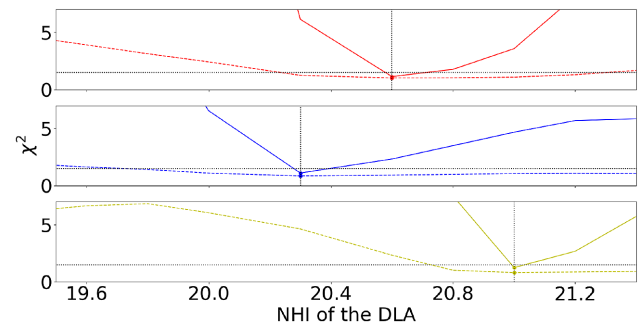

Figure 18. Minimum χ^2 as a function of the DLA column density for the different mock spectra obtained, from the top to bottom panel, using the spherical, the wind and the Keplerian disc model, respectively. In each panel, the minimum χ^2 evolution is plotted as a dashed line (resp. solid line) for spectra in LR (respectively HR). The black vertical dotted lines correspond to the input column densities. The thin black horizontal dotted lines correspond to the $\chi^2 = 1.5$ threshold.
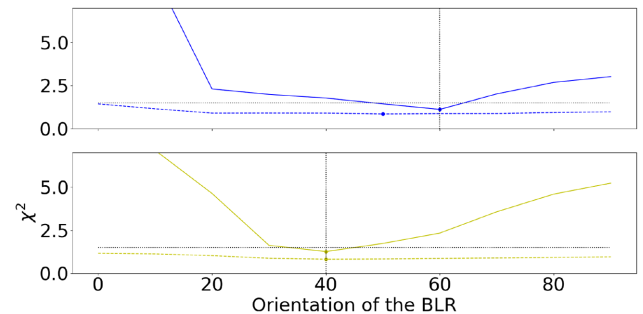

Figure 19. Minimum χ^2 as a function of the inclination of the BLR with respect to the observer for the wind model (top panel) and the disc model (lower panel) mock spectra. On each panel, the minimum χ^2 evolution is plotted as a dashed line (respectively solid line) for spectra in LR (respectively HR). The black vertical dotted lines correspond to the input inclination. The thin black horizontal dotted lines correspond to the $\chi^2 = 1.5$ threshold.

5.1 Column density of the absorbing cloud

As said before, when the redshift of the absorber is high enough, the DLA column density can be inferred from the absorption lines of the Lyman series. However, in most cases, only the Lyα line wavelength range is available.

Fig. 18 shows the minimum χ^2 as a function of the neutral column density for the three models in LR and HR. The minimum of each curve is indicated by a coloured dot.

In the three cases, the correct N(H I) value indicated by a vertical line is retrieved by the model that the mock spectrum is based on. The determination is more precise with high-quality data (HR).

5.2 Inclination of the BLR

Fig. 19 represents the minimum χ^2 as a function of the inclination angle with respect to the observer for the wind and the disc mock spectra. We do not use the spherical model as the later is symmetric and has no inclination parameter.

The minimum value of each curve is indicated by a coloured dot. We observe that the two curves have a minimum at the correct inclination of the BLR of their respective mock spectrum. However, the constraints are weak. Using the χ^2 threshold given before, we
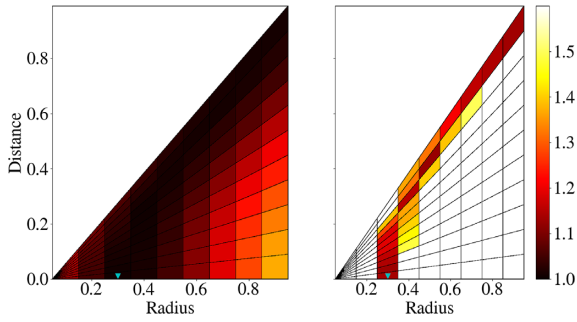
Figure 20. Maps representing the χ^2 as a function of the radius of the cloud and its distance to the centre for the mock spectra obtained using the spherical model in LR (left panel) and HR (right panel). The blue triangle indicates the radius and distance used to obtain the mock spectrum. The χ^2 colour scale is shown on the right-hand side of the figure.
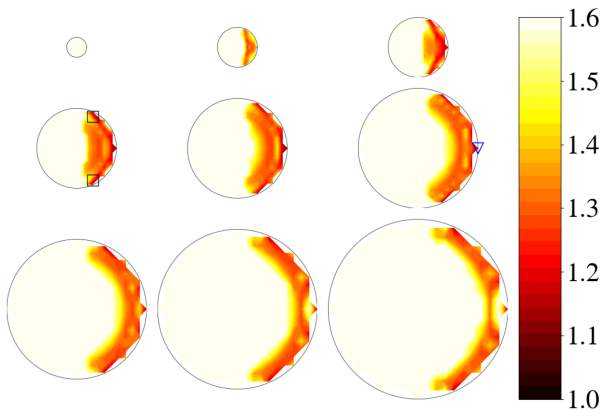

Figure 21. χ^2 as a function of the position and radius of the cloud in HR for the wind model. The best-fitting position is indicated by a blue triangle whereas the two possible input positions are indicated by two black boxes. There are two possible input positions due to the symmetry relative to the x-axis.

cannot constrain the inclination when fitting LR spectra. With HR spectra, the inclination is better constrained.

From this comparison, it is again clear that high-quality data are needed to constrain this parameter within a decent error box.

5.3 Size and position of the absorbing cloud

It is easy to foresee that the position and size of the absorbing cloud are degenerated parameters. The reason for this is that the emitting cloud density in the BLR is decreasing outwards. Two absorbing clouds with different radius can yield a similar spectrum provided the largest one is located further away from the centre because it will cover a larger but less dense region.

This is why for the three mock spectra with both resolutions, the minimum χ^2 as a function of the radius is almost constant and no clear minimum is seen.

Here again, we will fit the mock spectra with the model that has been used to construct it. The correlation between the cloud radius and its distance to the centre is illustrated in Fig. 20, showing the χ^2 as a function of those two parameters when using the spherical model. It is interesting to note that with high-quality data, it is possible to derive a lower limit of the radius, because the cloud must in any case cover the central region where the quasar continuum is emitted. In addition, the correlation between the distance to the centre and the
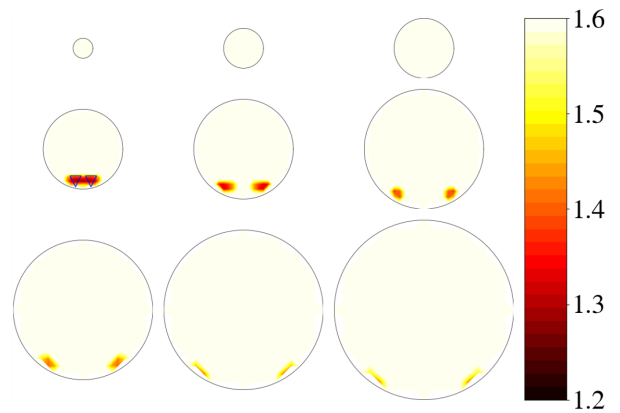
Figure 22. χ^2 as a function of the position and radius of the cloud in HR for the disc model. The best-fitting positions, which are also the input positions, are indicated by two blue triangles. There are two possible input positions due to the vertical symmetry.

radius of the cloud is tight, which means that the cloud cannot be much larger than its distance to the centre. This is a very interesting constraint as one could estimate independently the radius of the cloud by deriving the particle density in case C I absorption lines are detected (Fathivavsari et al. 2016).

For the wind and disc models, the χ^2 does not depend only on the radius and distance to the centre but also on the exact position of the cloud therefore its x and y coordinates. Fig. 21 shows the χ^2 at each position of the cloud for a radius varying from 0.1 on the top left-hand corner to 0.9 on the bottom right-hand corner with an increment of 0.1 when fitting the HR wind mock spectrum. In LR, almost all positions of the absorbing cloud give a good fit and it is possible to constrain neither the size nor the position. That is why only the HR version is discussed here. It is apparent that the radius and the distance to the centre are degenerated because tightly correlated for this model as well. For each cloud radius, the best fit is obtained with a cloud at a distance corresponding roughly to the radius. One can also notice that the right-hand side of the BLR is clearly favoured in the fit. This is due to the asymmetry of the absorption that favours one side of the model. Note that the model being symmetric relative to the x-axis, there are two possible input positions for the same mock spectrum.

For the disc model, we observe in Fig. 22(a) similar effect but even more apparent. Indeed, the locus of parameters yielding good fits is smaller and the radius can be constrained between 0.4 and 0.7 when the correct value is 0.4. We can also notice that the direction is pretty well constrained. This is investigated further in Fig. 23. This plot represents the minimum χ^2 as a function of the direction ϕ of the absorbing cloud with respect to the y-axis for different values of the radius. The minimum is reached with a direction of approximately $-76°$, which is the correct value represented by a black dotted line. At the other radius, the figure tends to show a preferred direction of $-60°$. This clearly shows that a preferred direction can be derived especially if the radius can be constrained independently from estimating the density using C I lines.

5.4 Summary

To summarize the results of the above exercise, we can conclude the following within the framework of the three models described above. (i) Not unexpectedly, high-quality data are preferred in all cases. (ii) The neutral hydrogen column density of the absorbing cloud can be estimated independently of the model used with reasonable precision
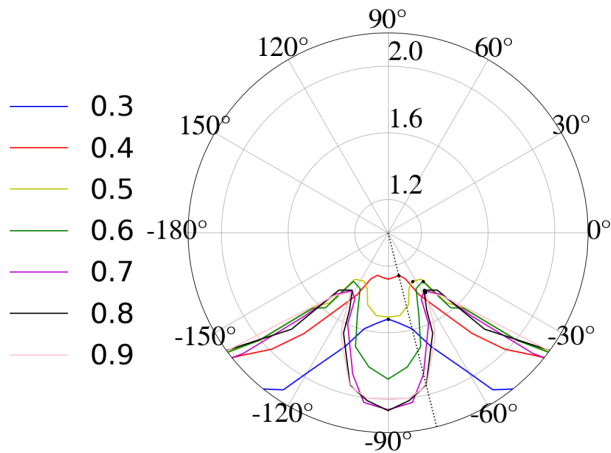
Figure 23. Curves (χ^2, ϕ) showing, for the wind model and each absorbing cloud radius, the minimum χ^2 found along the radial direction defined as the angle, ϕ, of the position of the cloud centre relative to the *y*-axis. The colour scale of the cloud radius is given on the left-hand side of the figure.

Figure 24. Best fit (red curve) of the Ly α emission of quasar J000958.66+015755.18 (black curve) with a wind model. The continuum, the BLR and NLR emissions are, respectively, the yellow, blue, and green curves.

Figure 25. Location of the BLR emitting clouds coloured as a function of their relative velocity for the best model of J000958.66+015755.18. The model is a wind model with inclination $i = 30°$. The absorbing cloud with radius $r = 0.6$ at location (0.4,0) is indicated by the black circle.

even with LR data. (iii) The radius and position of the absorbing cloud are degenerated. However, if the radius of the cloud can be estimated by an independent method, then the position of the cloud can be constrained. (iv) The radius of the cloud has to be larger but not much larger than the distance to the centre. For all other parameters, constraints are not strong and may be possible only if the best of the three models can be determined unambiguously.

6 FIT OF SDSS SPECTRA

In this section, we compare our models with observational data from the SDSS data release 12. We use the sample of *ghostly*-DLAs listed by Fathivavsari (2020). By definition a *ghostly*-DLA is characterized by the presence of strong metal lines, whereas the expected corresponding strong H I Ly α trough is not seen in the quasar spectrum. In some cases, no trace of the H I absorption can be seen. In that case, it is not possible, without any additional information to constrain our models. In other cases however, some residual of the H I absorption is left in the spectrum providing a direct access to the H I column density. Among the 23 *ghostly*-DLAs in the sample, 7 show some absorption residual. Among the seven spectra only three have a high enough S/N (S/N > 10) to perform a realistic fit with our models, QSO J000958.66+015755.18 having the highest S/N (S/N > 20).

6.1 Fit of QSO J000958.66+015755.18

The spectrum of QSO J000958.66+015755.18 has the highest S/N in the sample of *ghostly*-DLAs. In addition, the redshift of the quasar is $z_{QSO} = 2.973$, which means that the Ly β line is seen in the spectrum. The *ghostly*-DLA is at $z_{DLA} = 2.976\,35$, derived from the numerous strong metal absorption lines.

Before comparing the observations with our different models, we have to remove the N V contribution from the quasar emission. We fit a Gaussian emission located at $\lambda_{rest} = 1240.1$ Å and remove it from the spectrum. During the fit, we have excluded the pixels affected by strong absorptions unrelated to our system and located around -4000, -2000, and 6000 km s^{-1}.

The best fit of the QSO Ly α emission line is displayed in Fig. 24. The fit is a wind model with an inclination relative to the line of
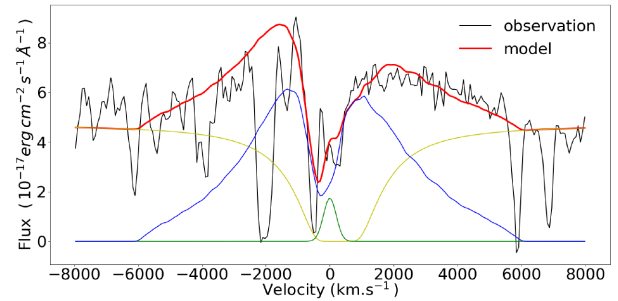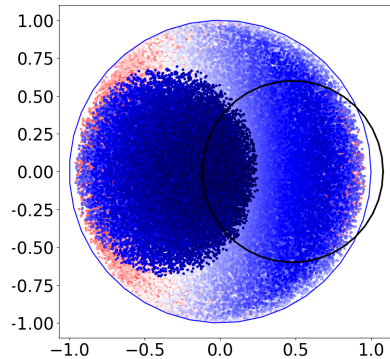
sight of 30°. The absorption cloud has a column density of log N(H I) = 20.8, a radius $r = 0.6$ and is located at (0.48, 0.0) (see Fig. 25). The redshift of the quasar studied here is high enough so that the Ly β absorption from the DLA is redshifted in the observed window. We therefore can use this line to confirm some of our findings. We use the best fit of the Ly α line and translate the model to Ly β.

For this, we adjust the continuum and add the Ly β and O VI $\lambda\lambda1031.9,1037.6$ doublet emissions. To model the Ly β emission, we consider the exact same emission clouds in the BLR as for Ly α. In addition, we assume that they also emit the O VI emission, i.e. the BLR has the same configuration for both species. Telfer et al. (2002) indicate that the Ly β and O VI blend has a flux of approximately 0.2 that of the Ly α one. In Somalwar et al. (2020), the authors present a quasar spectrum where the Ly β and O VI doublet emissions are not blended and have a flux equal to 2.5 per cent and twice 7.5 per cent of the Ly α emission, respectively. We use the latter numbers.

The only parameter that remains unknown, is the Ly β/Ly α flux ratio for the NLR. This ratio can vary between 1/3 and 1/30. To have an upper limit on the Ly β emission, we use a ratio of 1/3.

The result is presented in Fig. 26. The weakness of the line emission compared to the continuum explains easily why the absorption due to the DLA is detected in Ly β whereas it is not detected in Ly α. Note that the fit is good enough to confirm the H I column density derived from the fit of Ly α only. It can be seen that there is some flux residual at the bottom of the Ly β trough. With the quality of the
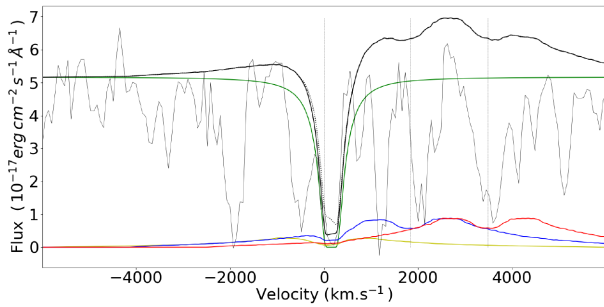
Figure 26. We extrapolate our model to Ly β with parameters constrained by the fit of the Ly α emission in quasar J000958.66+015755.18. The contributions of Ly β, and O VI $\lambda\lambda$1031.9,1037.6 are, respectively, the yellow, blue, and red solid lines The continuum is the green curve and the black solid line is the sum of all emission components. In grey, the spectrum of the observed QSO J000958.66+015755.18. The three vertical lines indicate the positions of the Ly β and O VI emission lines.
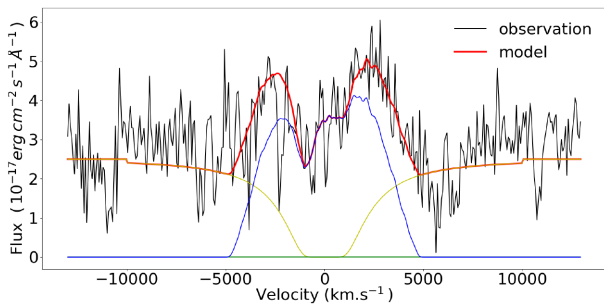
Figure 27. Best fit of the Ly α emission in the spectrum of QSO J124202.03−002209.00 (red curve) overplotted on to the data (black curve). The continuum, BLR, and NLR emissions are represented by, respectively, the yellow, blue, and green curves.

SDSS data, it is not possible to derive anything from it. However, using much better quality data (e.g. from XSHOOTER on the VLT), it would be possible to constrain better our model and especially the Ly α/Ly β emission ratios.

It is possible that the absorbing cloud bears some O VI that could absorb the BLR O VI emission and the quasar continuum. Due to the fact that Ly β is located in the Lyman forest, it is difficult to test this possibility but again better quality data at higher spectral resolution could probably probe the presence of O VI in the cloud.

6.2 *N*(H I) column densities

We selected two additional quasars the spectrum of which is good enough to try to fit the Ly α emission in order to derive a neutral hydrogen column density in the cloud. Here, we briefly present the fit of these quasar spectra.

QSO J124202.03−002209.00 has $z_{QSO} = 2.379\,25$ and $z_{DLA} = 2.3792$. The fit displayed in Fig. 27 shows that no narrow component is needed to reproduce the spectrum. The fit is a wind model with a $60°$ inclination and log *N*(H I) = 21.2.

QSO J125437.96+315530.84 has $z_{QSO} = 2.299$ and $z_{DLA} = 2.301$. The fit is presented in Fig. 28 and one can see that a narrow component is needed but its contribution is weak. The fit is a wind model with an inclination of $40°$ and log *N*(H I) = 21.4.

For the three *ghostly*-DLAs with good enough data in SDSS, we derive H I column densities of 20.8, 21.2, and 21.4. Although the

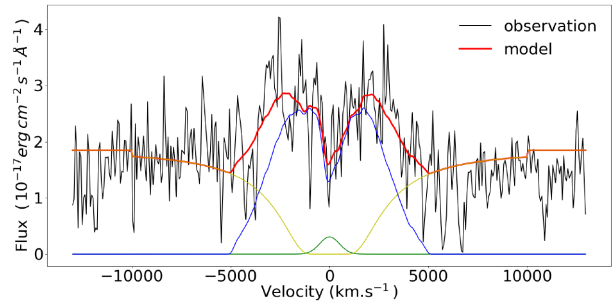**Figure 28.** Best fit of the Ly α emission in the spectrum of QSO J125437.96+315530.84 (red curve) overplotted on to the data (black curve). The continuum, BLR, and NLR emissions are represented by, respectively, the yellow, blue and green curves.

number is small this shows that indeed *ghostly*-DLAs are *bona fide* damped Ly α systems with log *N*(H I)>20.3. We note also that the three quasars are best fitted with the wind model.

7 CONCLUSION

We have constructed three geometrical models for the quasar BLR spatial and kinematical structures. The three models can reproduce the typical shape of the quasar Ly α emission. Adding an absorption cloud in front of the BLR, we have used these models to obtain mock spectra of so-called *ghostly*-DLAs. These absorbers are characterized by the presence of strong metal lines but no Ly α trough is seen in the quasar spectrum, indicating that although the region emitting the continuum is covered by the absorbing cloud, the BLR is only partially covered. We generate mock spectra with similar characteristics as good SDSS data (S/N = 10 and spectral resolution R = 2500) but also with higher S/N and spectral resolution, S/N = 50 and R = 5000.

We then try to recover the initial parameters by fitting the mock data. We show that the H I column density can be recovered precisely even in SDSS data. The size of the absorbing cloud and the distance to the centre are correlated and thus impossible to disentangle without any additional information. Only a minimal radius can be determined.

By comparing our models to SDSS data of observed *ghostly*-DLAs, we show that the H I column densities are large and in any case larger than 20.3. Even though the models can fit the observations, little information can be extracted with confidence with this data quality. However, we noticed that the wind and disc models are more versatile than the spherical one and can be more easily adapted to the observations.

We show that more constraints could be obtained from better quality data with higher S/N and spectral resolution, especially if the Ly β line can be observed. In particular, it seems possible to discriminate somehow between the three models. Further observations with higher resolution are required to investigate these fascinating objects.

DATA AVAILABILITY

Data used in this paper are from SDSS DR12 (Vanden 2001) and are publicly available at https://dr12.sdss.org/.

REFERENCES

Bentz M. C. et al., 2013, ApJ, 767, 149
Braibant L., Hutsemékers D., Sluse D., Goosmann R., 2017, A&A, 607, A32
Christensen L., Jahnke K., Wisotzki L., Sánchez S. F., 2006, A&A, 459, 717
Done C., Krolik J. H., 1996, ApJ, 463, 144
Du P. et al., 2016, ApJ, 820, 27
Fathivavsari H., 2020, ApJ, 888, 85
Fathivavsari H., Petitjean P., Zou S., Noterdaeme P., Ledoux C., Krühler T., Srianand R., 2016, MNRAS, 466, L58
Finley H. et al., 2013, A&A, 558, A111
Giustini M., Proga D., 2019, A&A, 630, A94
Gravity Collaboration et al., 2018, Nature, 563, 657
Grier C. J. et al., 2017, ApJ, 851, 21
Hamann F., Chartas G., Reeves J., Nardini E., 2018, MNRAS, 476, 943
Hennawi J. F., Prochaska J. X., Kollmeier J., Zheng Z., 2009, ApJ, 693, L49
Hutsemékers D., Braibant L., Sluse D., Goosmann R., 2019, A&A, 629, A43
Matthews J. H., Knigge C., Higginbottom N., Long K. S., Sim S. A., Mangham S. W., Parkinson E. J., Hewitt H. A., 2020, MNRAS, 492, 5540
Netzer H., 2008, New Astron. Rev., 52, 257
O'Sullivan D. B., Martin C., Matuszewski M., Hoadley K., Hamden E., Neill J. D., Lin Z., Parihar P., 2020, ApJ, 894, 3
Pancoast A., Brewer B. J., Treu T., 2014, MNRAS, 445, 3055
Pâris I. et al. 2018, A&A, 613, 17
Rankine A. L., Hewett P. C., Banerji M., Richards G. T., 2020, MNRAS, 492, 4553
Schneider P., Wambsganss J., 1990, A&A, 237, 42
Shen Y. et al., 2019, ApJ, 883, L14
Somalwar J., Johnson S. D., Stern J., Goulding A. D., Greene J. E., Zakamska N. L., Alexandroff R. M., Chen H.-W., 2020, ApJ, 890, L28
Telfer R. C., Zheng W., Kriss G. A., Davidsen A. F., 2002, ApJ, 565, 773
van de Voort F., Schaye J., Altay G., Theuns T., 2012, MNRAS, 421, 2809
Vanden Berk D. E. et al., 2001, AJ, 122, 549

This paper has been typeset from a TEX/LATEX file prepared by the author.